Tuning bimetallic catalysts for a selective growth of SWCNTs

Salomé Forel, Alice Castan, Hakim Amara, Ileana Florea, Frédéric Fossard, Laure Catala, Christophe Bichara, Talal Mallah, Vincent Huc, Annick Loiseau, et al.

Tuning bimetallic catalysts for a selective growth of SWCNTs

Article · February 2019

CITATIONS
0

READS
119

11 authors, including:

Salome Forel
École Polytechnique
6 PUBLICATIONS **2** CITATIONS
SEE PROFILE

Alice Castan
The French Aerospace Lab ONERA
8 PUBLICATIONS **70** CITATIONS
SEE PROFILE

Hakim Amara
The French Aerospace Lab ONERA
67 PUBLICATIONS **1,309** CITATIONS
SEE PROFILE

Florea Ileana
Laboratoire de Physique des Interfaces et des Couches Minces, Ecole Polytechnique
72 PUBLICATIONS **919** CITATIONS
SEE PROFILE

Journal Name

ARTICLE TYPE

Cite this: DOI: 10.1039/xxxxxxxxxx

Tuning bimetallic catalysts for a selective growth of SWCNTs

Salomé Forel,*[a] Alice Castan,*[b,c] Hakim Amara,*[b] Ileana Florea,[a] Frédéric Fossard,[b] Laure Catala,[c] Christophe Bichara,[d] Talal Mallah,[c] Vincent Huc,[c] Annick Loiseau,[b] and Costel-Sorin Cojocaru[a]

Received Date
Accepted Date

DOI: 10.1039/xxxxxxxxxx

www.rsc.org/journalname

Recent advances in structural control during the synthesis of SWCNTs have in common the use of bimetallic nanoparticles as catalysts, despite the fact that their exact role is not fully understood. We therefore analyze the effect of the catalyst's chemical composition on the structure of the resulting SWCNTs by comparing three bimetallic catalysts (FeRu, CoRu and NiRu). A specific synthesis protocol is designed to impede the catalyst nanoparticle coalescence mechanisms and stabilize their diameter distributions throughout the growth. Owing to the ruthenium component which has a limited carbon solubility, tubes grow in tangential mode and their diameter is close to that of their seeding nanoparticle. By using as-synthesized SWCNTs as a channel material in field effect transistors, we show how the chemical composition of the catalysts and temperature can be used as parameters to tune the diameter distribution and semiconducting-to-metallic ratio of SWCNT samples. Finally, a phenomenological model, based on the dependence of the carbon solubility as a function of catalyst nanoparticle size and nature of the alloying elements, is proposed to interpret the results.

1 Introduction

During the last decades, single-walled carbon nanotubes (SWCNTs) have been the focus of an intense research effort, highlighting their exceptional mechanical, electronic, optical and thermal properties[1]. In the field of nanotechnology, what appears today as the weak link for further application of carbon nanotubes is the difficulty to obtain large quantities and high purity of a unique structure of carbon nanotubes. Indeed, according to its structure, a nanotube can be metallic or semiconducting with a large range of gaps, depending on its diameter. Up to now only few chiralities have been obtained through selective synthesis ((6,5)[2–6], (9,8)[7], (6,6)[8], (12,6)[9,10], (16,0)[11], (8,4)[10], (14,4)[12]) but only the (6,6) synthesis has been reported to be 100 % selective, albeit with a very poor yield. In the latter cases, the use of post-synthesis sorting is still needed. Importantly most of the cited syntheses focused on the use of bimetallic catalyst nanoparticles (NPs)[2–4,6,7,9]. Several hypotheses, supported by theoretical studies have been put forward to explain this chiral selectivity[13–19] but none of them have been unanimously accepted.

In the absence of a routine synthesis technique able to provide single-chirality SWCNT samples, various ways aiming at controlling the electronic properties of carbon nanotubes have been investigated[20], especially to favor the growth of semiconducting SWCNTs (s-SWCNTs), highly desired for applications in microelectronics. Two main routes are used: the selective etching of metallic SWCNTs (m-SWCNTs) during the growth process[21–26], or the burning of m-SWCNTs after integration into a device[27]. Nevertheless, obtaining s-SWCNT-enriched samples is not sufficient for designing efficient devices: a fine-tuning of the diameter of the SWCNTs, which is inversely proportional to the gap, can greatly contribute to improving device performance[26]. To this aim, the most common method relies on a fine control of the catalyst NP size where different assumptions are generally proposed. First, such control is constrained by coalescence mechanisms, which are highly activated at the temperature used in the chemical vapor deposition (CVD) process (600-1200°C). Indeed, many groups reported a global increase of nanotube diameters upon increase of the growth temperature, often explained in

[a] Laboratoire de Physique des Interfaces et des Couches Minces, CNRS, Ecole Polytechnique, 91128, Palaiseau Cedex, France ; E-mail: salome.forel@polytechnique.edu
[b] Laboratoire d'Etude des Microstructures, ONERA-CNRS, UMR104, Université Paris-Saclay, BP 72, 92322 Châtillon Cedex, France ; E-mail: alice.castan@onera.fr, hakim.amara@onera.fr
[c] Institut de Chimie Moléculaire et des Matériaux d'Orsay, CNRS, Université Paris-Sud/Paris-Saclay, 15 rue Georges Clemenceau, Orsay, France
[d] Aix Marseille Univ, CNRS, CINAM, Marseille, France

† Electronic Supplementary Information (ESI) available: [details of any supplementary information available should be included here]. See DOI: 10.1039/b000000x/

terms of catalyst coarsening leading to the disappearance of the smallest-sized catalyst particles, and subsequently of the small diameter SWCNTs[28–31]. This phenomenon, although likely to appear, was rarely demonstrated. The control of nanotube diameters is also explained by selective activation or deactivation of catalyst particles through their size. This selective activation is reportedly driven by the chemical interaction between carbon and the metal of the particle which strongly depends both on the catalyst size/nature and the growth temperature[32–36].

Whatever the hypothesis put forward, these reported mechanisms imply that catalyst NP size and SWCNT diameter are very closely linked, which is not always the case. Indeed, two growth modes can be envisioned during a given growth event: a tangential growth mode where the diameter of the NP and the resulting nanotube are similar, and a perpendicular mode where they are no longer related[37]. Moreover, for iron, nickel or cobalt catalysts, these modes have been shown to depend on the wetting or dewetting properties of the carbon wall with respect to the catalyst surface, which are themselves driven by the fraction of carbon dissolved inside the catalyst[38,39].

It is therefore obvious that the control of the chemical state of the catalyst NP in interaction with carbon precursors is a key factor for producing nanotubes with defined diameters. As a result, our approach relies first on favoring a tangential growth mode so that SWCNT diameters are governed by catalyst sizes, and suppressing catalyst coalescence mechanisms to get a good control of their sizes. In this context, we conducted a systematic study of our growth process by modulating the carbon solubility properties in the catalyst NPs by using different chemical compositions (FeRu, CoRu and NiRu) whose thermodynamic properties with respect to carbon are different, and performing growths at various temperatures. Under these conditions, a better understanding of the SWCNT growth mechanism is possible, resulting in more selective syntheses, with a better diameter control coupled with an increase of the semiconducting-to-metallic ratio.

2 Results and discussion

2.1 Nanoparticle analysis

For this study, we adapted the chemical composition of the catalyst in order to obtain catalysts with different chemical behaviors with respect to carbon, and to favor a tangential growth mode. We set our choice of catalysts on iron, cobalt and nickel mixed with ruthenium. Iron, cobalt and nickel have been chosen for their well-known ability to seed the growth of SWCNTs and for their different chemical affinities for carbon. Indeed, as a general trend for transition metals, carbon affinity decreases from the left to the right of the periodical table. In the bulk, carbon solubility is found to be around 0.3-0.5 at. % in Ni, 1.2 at. % in fcc-Co at 700°C, and around 4 at. % for γ-Fe at 800°C[13]. Alloying these metals with ruthenium is expected to lower the carbon solubility limit (at 700°C, the carbon solubility in bulk ruthenium is around 0.15 at. %[40]) and therefore to favor the tangential growth mode according to[39] and to increase the melting temperature[41,42] such as to maintain the alloy NPs in a solid state at the CVD growth temperatures. We therefore anticipate that employing these alloys fosters a tangential growth mode on a solid catalyst.

To produce bimetallic NPs (Fe-Ru, Co-Ru and Ni-Ru) with predefined compositions close to 1:1, we used a new SWCNT synthetic processes that we recently reported[43], based on Prussian blue analogs (PBAs)[44] as catalyst precursors (see Methods section). This approach was shown to produce truly alloyed NPs with controlled and tunable chemical composition and also uniform size around 1.5 nm well-adapted to the growth of SWCNTs. Details on the extensive characterization of the precursors and effective catalysts used for this study can be found in the electronic supporting information (ESI) and in ref[43] (see Fig.1, and Figs. S1 and S2 in the ESI).

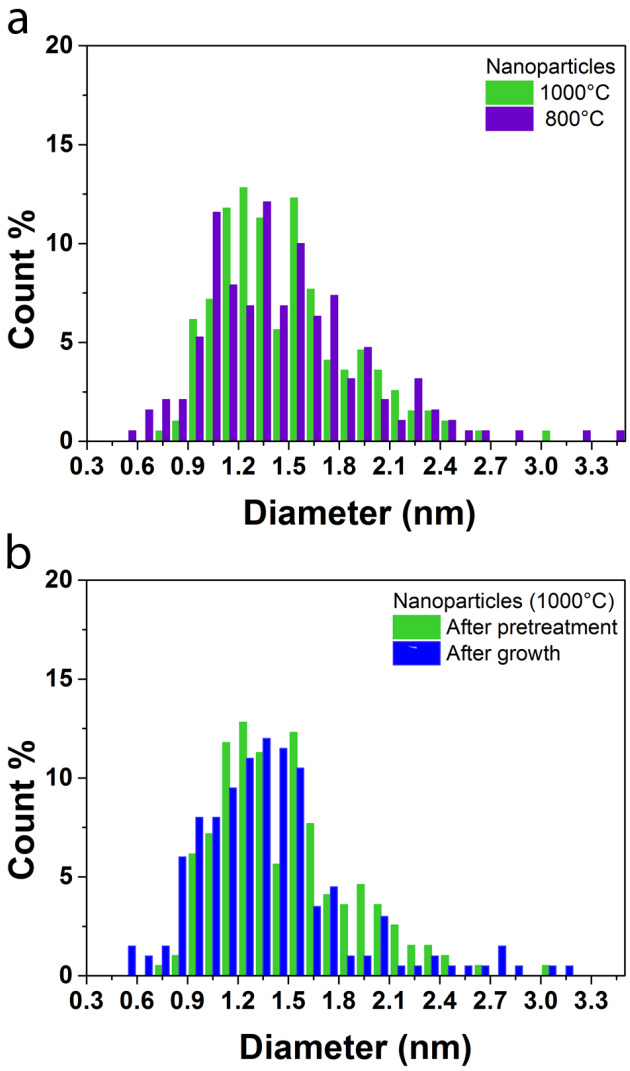

Fig. 1 (a) Size distribution histograms of FeRu NPs after pretreatment at 800°C (purple), and 1000°C (green), (b) Size distribution histograms of FeRu NPs after the 5-minute pretreatment (green), and after growth (blue) at 1000°C (statistics on 200 NPs).

On the path to analyzing the effect of temperature on SWCNT growth, one of the major obstacles is related to coarsening and coalescence phenomena, such as Ostwald ripening[45] which is a thermally activated process. As previously described, many stud-

ies in the literature reported an increase of the as-grown SWCNT diameters at higher temperature due to an increase of the mean catalyst size induced by a coarsening mechanism[28–31]. In the proposed synthesis method, the activation of the coalescence mechanism is expected to be highly impeded. First, thanks to an appropriate surface chemical functionalization of the support substrate, the catalyst density has been shown to be limited to one monolayer.[43] Second, using highly activated hydrogen induces surface defects on the substrate with high-trapping energy over the substrate[46]. These defects limit the surface diffusion of the catalyst metal atoms and increase the pinning effect of the forming NPs[43,46,47].

In order to verify such unusual limited coalescence, we compared, using statistical transmission electron microscopy (TEM) measurements (around 200 NPs counted for each sample), the size distribution of the catalyst NPs after the pretreatment step preceding their exposure to the carbon gas source at 800°C and 1000°C. As an example, the case of FeRu is discussed here whereas results for other alloys can be found in Fig. S1 in the ESI. Fig. 1a presents the size distribution histograms of FeRu NPs after the five-minute pretreatment conducted in the CVD reactor at 800°C and 1000°C, respectively. The obtained size distributions are very similar. In both cases, small NPs are mostly present over the surface, 57 % of counted NPs are below 1.5 nm at 800°C, and 56 % at 1000°C. These measurements let us assume that during the SWCNT synthesis process, after the 5-minute pretreatment, when the carbon feed is introduced, the same population of catalytic NPs is available for subsequent SWCNT growth. Furthermore, to ensure that the coalescence does not occur after the introduction of methane and during the 30 minutes of SWCNT growth, we also compared the catalyst size distributions after the pretreatment step and respectively after SWCNT growth. As presented in Fig. 1b, for the synthesis process at 1000°C, the highest temperature in this study, and for which it is reasonable to expect the highest activation of the coalescence mechanisms, the catalyst diameter distributions are very similar after the pretreatment step and after the half-hour growth, and only extremely limited traces of coalescence can be observed. Similar results for all three catalysts, but for a synthetic process at 800°C have been already demonstrated[43].

2.2 Tube/catalyst interaction

We now focus on the diameter distribution of the tubes grown by performing systematic investigations of the growth temperature influence for the three types of nanoalloy catalysts at 700°C, 800°C, 900°C, and 1000°C, respectively. The SWCNT diameter distributions were investigated through Raman spectroscopy with four excitation wavelengths (see Methods section). Fig. 2 represents the results obtained for one batch of samples (see Fig. S3 in the ESI).The yield of the syntheses (Fig. S4) and the reproducibility of the results for the FeRu system (Fig. S5) are discussed in the ESI.

Contrary to the particle diameters, the detected SWCNT diameters are clearly temperature-dependent and following the same trend, whatever the catalyst (see Figs. 2a-c), even if one can note

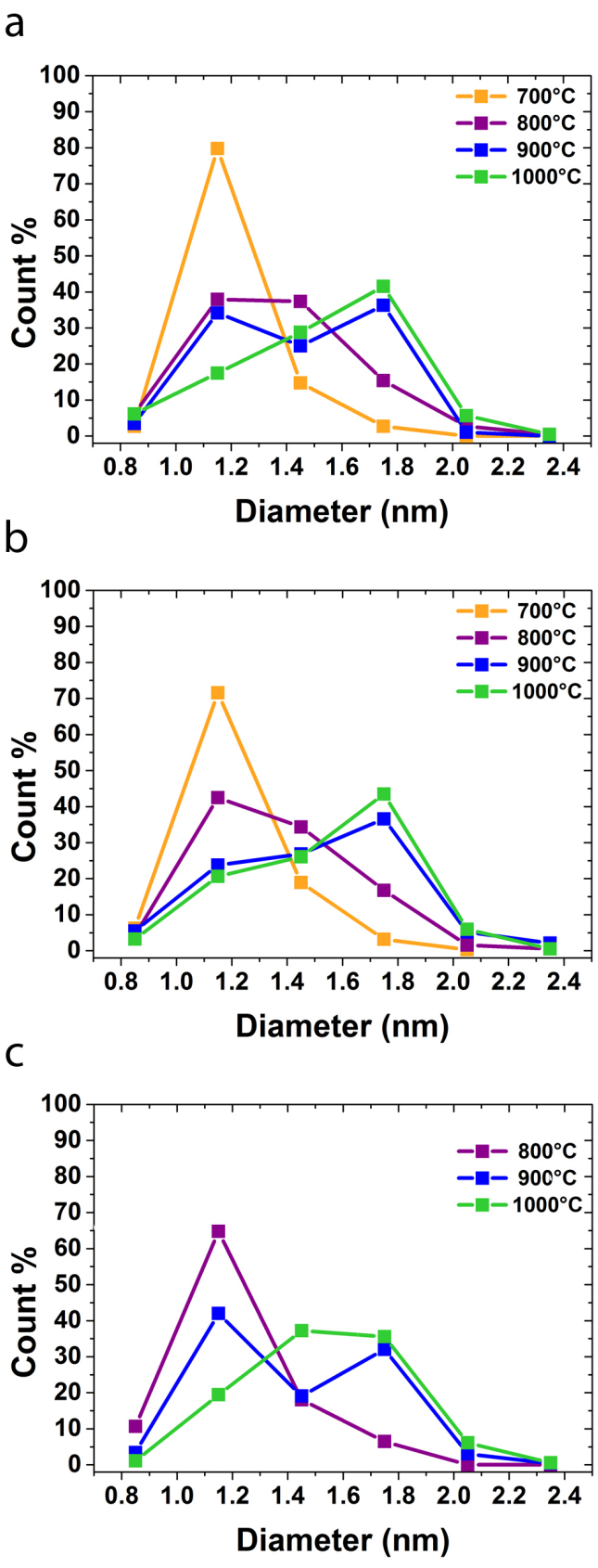

Fig. 2 Diameter distributions obtained through Raman spectroscopy analysis for growths from (a) FeRu catalysts, (b) CoRu catalysts, and (c) NiRu catalysts. The point is placed in the middle of each diameter bin (0.3 nm wide).

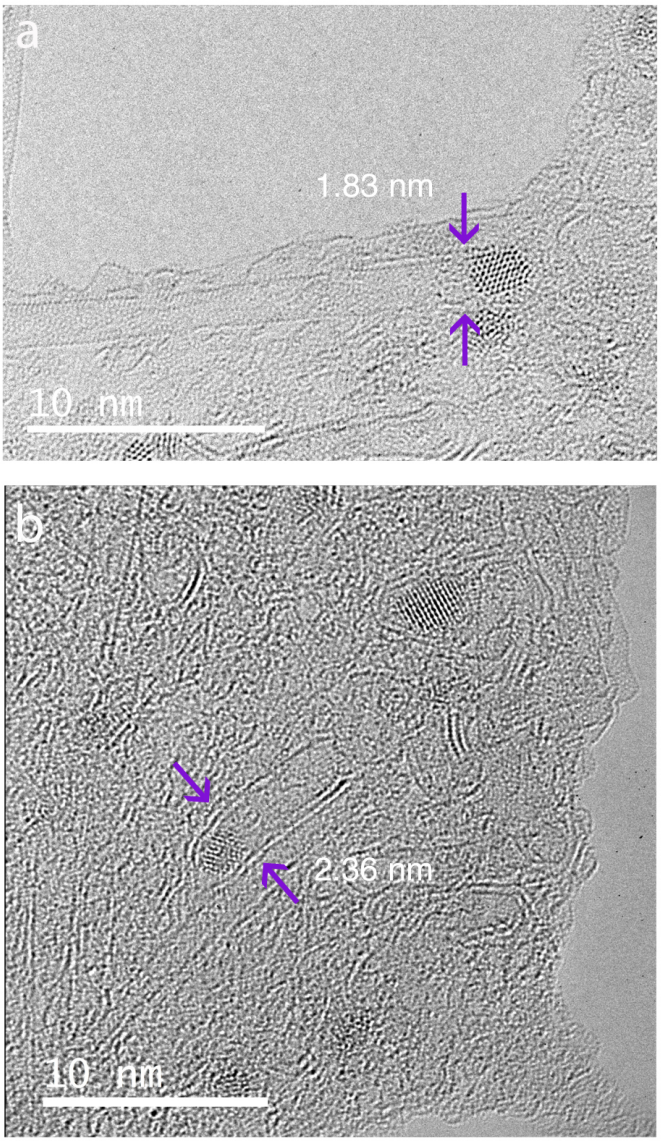

Fig. 3 High resolution TEM (HRTEM) images of nanotubes attached to their corresponding catalyst NPs in the cases of growths from (a) the CoRu catalyst at 800°C and (b) from the FeRu catalyst at 800°C (bottom), both in a tangential growth configuration. The diameters of the SWCNTs shown here are not representative of the most abundant diameters in our syntheses (according to Raman spectroscopy analysis), but present the advantage to clearly show occurrences of the tangential growth configuration. More representative SWCNT TEM images are available in the ESI (Figs. S6 and S7).

that nanotubes could not be grown at 700°C for the NiRu catalyst system, and were only observed at 800°C and above, this point will be discussed later. At low temperatures (700°C for the FeRu and CoRu systems, or 800°C for the NiRu system), a majority of small diameter SWCNTs are synthesized and very few larger diameter nanotubes were observed. For instance, for each of the three catalysts, when the growth is performed at the lowest temperature (700°C for FeRu and CoRu catalyst or 800°C for NiRu catalyst), more than 65 % of the counted SWCNTs have diameters below 1.3 nm, and fewer than 6 % have diameters above 1.6 nm. Upon temperature increase, the number of small-diameter SWCNTs decreases whilst the number of larger diameter SWCNTs increases. At 1000°C, less than 23 % of the nanotubes are found to have diameters below 1.3 nm and more than 40 % above 1.6 nm.

The next step was to examine the growth mode in order to determine the origin of the temperature dependence of SWCNT diameters. In all cases where a nanotube was seen attached to its catalyst NP during our TEM investigations, the observed growth mode was systematically the tangential type independently of the NP diameter (see Fig. 3). This finding reasonably validates our approach in designing a catalyst to privilege a tangential growth by tuning the carbon concentration in the NP. Importantly, if we consider the diameters of the NP and the attached nanotube to be close to equal, the small NPs appear to be less active for growth at 1000°C, while bigger NPs are less active at low temperature (see Fig. S8 in the ESI). To confirm a selective activation of the available NPs with temperature, we have performed the SWCNT growth at 800°C, but starting with catalyst NPs pretreated five minutes at 1000°C (see Fig. S9 in the ESI). The SWCNT diameter distribution is similar to those obtained for a full synthesis procedure at 800°C, supporting a selective activation well related to the growth temperature.

We can therefore conclude that catalyst NPs available for synthesis are roughly in the same size range whatever the growth temperature, but that they are selectively activated according to their size, leading to SWCNTs of different diameter ranges as a function of temperature.

2.3 Phenomenological model

It is commonly admitted that SWCNT growth can start only after the carbon saturation of the corresponding catalyst NP has been reached[38,48–50]. In the particular context of nanotube growth, theoretical studies forecast an increase of carbon solubility with the decrease of the NP size, which can affect the growth mechanism[35,36,51,52]. Experimentally, Picher and co-workers[33,34] reported that at high growth temperatures in the low pressure domain, small catalyst NPs were not activated due to a higher supersaturation limit as compared to that of the larger particles in agreement with[53]. This hypothesis could be used to explain the lack of small diameter SWCNTs observed at high temperatures, but does not seem to be very realistic within the frame of our specific growth conditions. Indeed, the partial pressure of methane is relatively high (around 27 mbar) and the synthesis time is relatively long (30 minutes), it seems difficult to envision a possible lack of sufficient carbon feed of the catalyst as a limiting factor. Besides, recently published calculations on SWCNT growth from NPs with various carbon concentrations highlighted its influence on the nanotube's nucleation[54]. In the case of a catalyst with a low carbon concentration, a strong adhesion between the initially formed carbon sp^2 cap and the NP is expected, leading to their poisoning. On the contrary, it is found that the high-carbon concentrations metal NPs present an insufficient adhesion towards the nanotube, inducing the SWCNT growth termination.

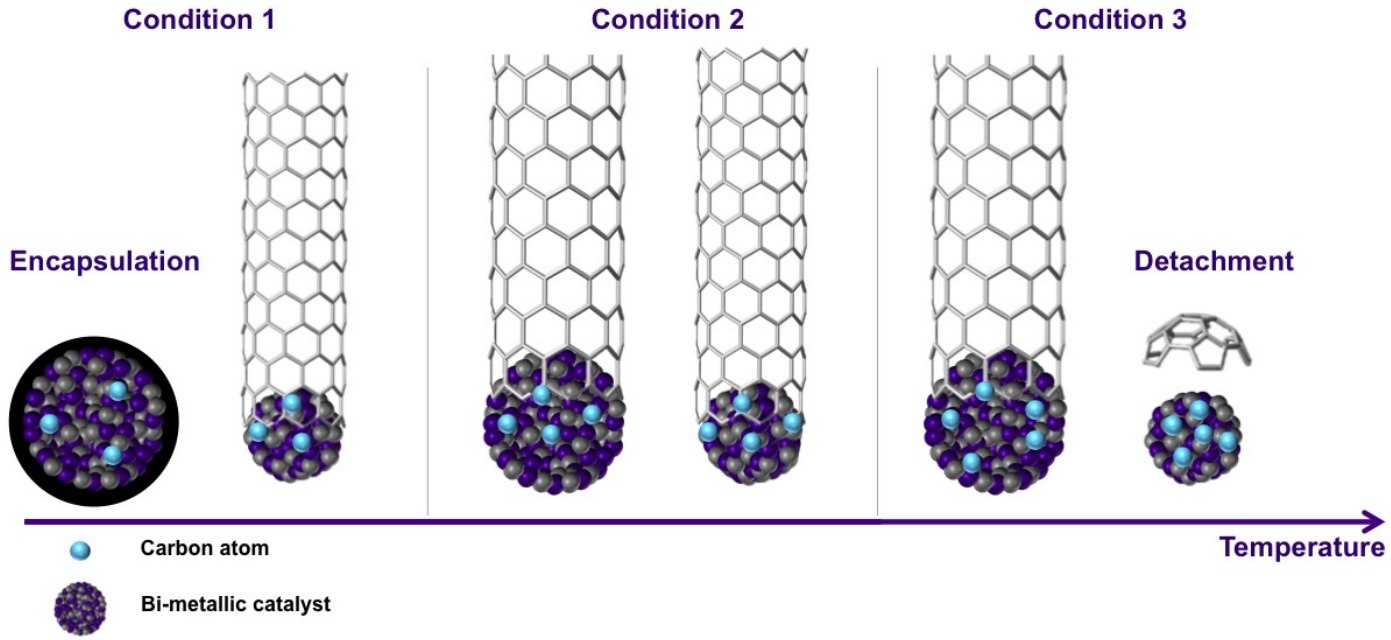

Fig. 4 Schematic view of the proposed mechanism of selective activation of catalyst NPs based on growth temperature and NP size.

On the basis of all these considerations, we propose a growth process sketched in a simplified scheme in Fig. 4 to account for our experiments. The key point is to distinguish two kinds of NPs depending on their size: "small" versus "large" NPs. Using this crude separation, we propose to explain the catalyst size selectivity as follows. At low temperatures, the carbon fraction of larger particles is low. According to calculations done in[54], this lack favors a strong adhesion of the sp^2 layer on the catalyst surface which leads to the encapsulation and deactivation of the NP (condition 1 in Fig. 4). On the contrary due their higher carbon fraction, small catalyst NPs tend to favor the dewetting of the sp^2 cap formed on their surface and are capable of initiating the SWCNT growth. When the growth temperature increases, carbon solubility in larger NPs increases and gets high enough to allow the lift-off of the sp^2 cap (condition 3 in Fig. 4). In turn, the carbon solubility in smaller NPs also increases but too much, and can induce a detachment of the carbon cap so rapid that it prevents the nanotube growth initiation (condition 3 in Fig. 4). In the intermediate temperature range, the carbon solubility limit of both smaller and bigger catalyst NPs are propitious to nanotube growth initiation (condition 2 in Fig. 4).

The present phenomenological model of the temperature dependence of carbon solubility in NPs relatively to their size accounts well for the general trend regarding the evolution of SWCNT diameter distributions observed in Fig. 2. Indeed, in view of the data for the FeRu catalyst system, we first observed at low temperature the growth of small SWCNTs (in line with condition 1 in Fig. 4). Many encapsulated catalyst NPs can be seen on post-growth TEM images of the samples (see Figs. S6 and S7 in the ESI), however there is no way to determine whether this encapsulation occurred during the growth process, or upon cooling of the sample after CVD growth. This means that a statistical analysis of the presence or absence of a graphitic shell around catalyst NPs with respect to their size would be erroneous by post growth TEM analysis, that is why we choose not to mention it. Then, when the temperature increases, a combination of small and larger tubes is obtained (in line with condition 2 in Fig. 4). And finally for the highest temperature a majority of large nanotubes are grown (in line with condition 3 in Fig. 4). Few differences are observed between the growth from the FeRu and CoRu catalysts, but a clear difference appears with the NiRu catalyst system where no SWCNT growth is observed at the lowest temperature 700°C. Referring back to our model, a lower carbon solubility in the NiRu catalyst as compared to the two other alloys can explain such a result. At the lowest tested temperature (700°C), carbon solubility in the NiRu NPs in the available diameter range is too low to induce a growth of SWCNTs. As the temperature increases, the carbon solubility increases and the NPs are gradually activated through their size : first the smaller then the bigger ones, until the occurrence of the deactivation of the smaller size ones at high temperature (1000°C). However, assuming a temperature upshift of 100°C, between NiRu and (Fe/Co)Ru, SWCNT diameter distributions get quite comparable. This lower carbon solubility in NiRu is nicely consistent with the relative carbon solubility in the corresponding bulk materials, that is ten times lower in nickel as compared to cobalt and iron, the presence of ruthenium seems therefore significantly enhances this effect.

2.4 Impact of the nanotube diameter distribution control on the SC/M ratio

The ability to control and choose the diameter of the growing SWCNT previously discussed can now be exploited to favor a tunable enrichment of the semiconducting or metallic SWCNT populations in the samples. Indeed, it has been shown that the use of an etching gas to obtain s-SWCNT enrichment during CVD

growth seems to be efficient only in a specific diameter range (typically above 1.4 nm) [22–26]. For smaller diameters (< 1.4 nm), no selective etching of the m- and s-SWCNTs was observed. Li and co-workers reported a similar diameter dependence trend when using hydrogen as an etching gas [25]. Here we show that our catalyst family is not only capable of allowing SWCNT growth with selective diameter distribution but also with selective semiconducting/metallic character.

To that end, we used Raman spectroscopy data to determine the SC/M ratio of our SWCNT samples (see Methods section for more detail). As seen in Fig. 5, we can clearly observe an increase in the percentage of s-SWCNTs with the temperature for all catalysts. This selectivity is explained first by the activated hydrogen used during the synthesis, which acts as an efficient etching agent, and second by the fact that at high temperature tube diameters range above 1.4 nm, the lower limit above which etching is efficient.

To prove the efficiency of our method for growing SWCNTs with a selectivity in diameter and SC/M ratio, we integrated the as-synthesized SWCNTs as a channel material in field effect transistors (FETs) (see Fig. S10 in the ESI for a schematic view of the device) and subsequently statistically analyzed their electrical characteristics. This measurement also allows cross-checking of the Raman spectroscopy measurements. As we performed the SWCNT growth experiments on SiO_2/Si wafers, the as-obtained SWCNTs can directly be integrated in bottom gate SWCNT-FET device structures without transfer steps (see Methods section). As very few SWCNTs were observed for the growth from the NiRu catalyst at 700°C, we chose to use nanotubes grown from the three catalysts types at two extreme growth temperatures, respectively 800°C and 1000°C. Over fifty devices were characterized for each starting catalyst type and growth temperature. We will focus the analysis on the On-current value and the Ion/Ioff ratio value for the as-fabricated device, before and after a breakdown process (see Methods section), which is intended to disconnect the metallic SWCNTs present in the FET channel.

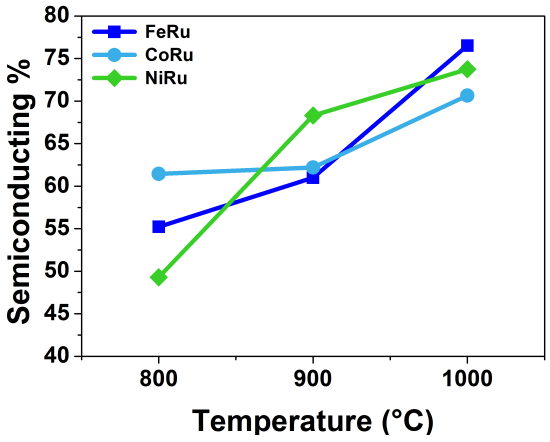

Fig. 5 Evolution of the percentage of s-SWCNTs determined by Raman spectroscopy analysis for the three catalysts at various growth temperatures.

Before applying the breakdown process (blue points in Fig. 6), for all devices, we observe a similar trend as a function of the SWCNT growth temperature, independent of the catalyst type. When SWCNTs grown at the lowest temperature are integrated in a transistor channel (Fig. 6 and Fig. S11 in the ESI), a majority of the devices are found to be ineffective (i.e. Ion/Ioff ratio lower than 10). For SWCNTs grown at high temperature (Fig. 6 and Fig. S11 in the ESI), however, few of the fabricated transistors are ineffective.

One can observe that electrical breakdown of all the measured transistors has only a limited effect on transistors integrating nanotubes grown at 1000°C. As shown in Fig. 6, a very weak improvement of the Ion/Ioff ratio is obtained and the On-current stays relatively constant. We calculated the percentage of transistors presenting an improvement of Ion/Ioff ratio larger than 3 decades after the electrical breakdown (see Fig. S11 in the ESI). For instance, such improvement concerns 6 % of transistors made with nanotube synthetized from FeRu at 1000°C which is not significant. We therefore conclude that only a weak proportion of m-SWCNTs connects source and drain, again confirming the s-SWCNT enrichment detected through Raman spectroscopy. On the contrary, the electrical breakdown appears to be very effective for transistors made from SWCNTs grown at 800°C. After the breakdown, for each of the transistors with 800°C grown nanotubes, the Ion/Ioff ratio increased and the On-current decreased. Here, an improvement of the Ion/Ioff ratio superior to 3 decades is around 28 % for the transistors with SWCNTs grown at 800°C from FeRu (see Fig. S11 in the ESI). Such results are expected when the contribution of m-SWCNTs is suppressed. This result highlights a higher contribution of m-SWCNT to this type of transistors, consistent with the Raman characterization.

Further insights are expected to be retrieved after applying the breakdown process for disconnecting metallic conducting paths from the FET channels. Particularly the electronic band gap of s-SWCNTs being diameter-dependent, the Off-current value is expected to increase as the nanotube's bandgap decreases (as the Schottky barrier height at contacts is expected to decrease and consequently unwanted tunneling carrier injection increases). Then, after electrical breakdown, transfer characteristics obtained for FET devices based on SWCNTs grown at 800°C should present higher Ion/Ioff ratios. This behaviour is indeed well visible in Fig. S12 in the ESI which shows the Off-current obtained in all the measured transistors after electrical breakdown as a function of the Ion/Ioff ratio, confirming that smaller SWCNTs have been obtained for this lower temperature growth. Finally, it is important to note that despite the simplicity of the transistor design, our synthesis method allows to easily obtain transistors with good Ion/Ioff ratios. Indeed, Ion/Ioff ratios larger than eight decades for the best ones, and around five decades on average have been obtained. These performances are on the same order of magnitude as the best devices obtained using random percolating networks of SWCNTs as channel reported in the literature [55–57].

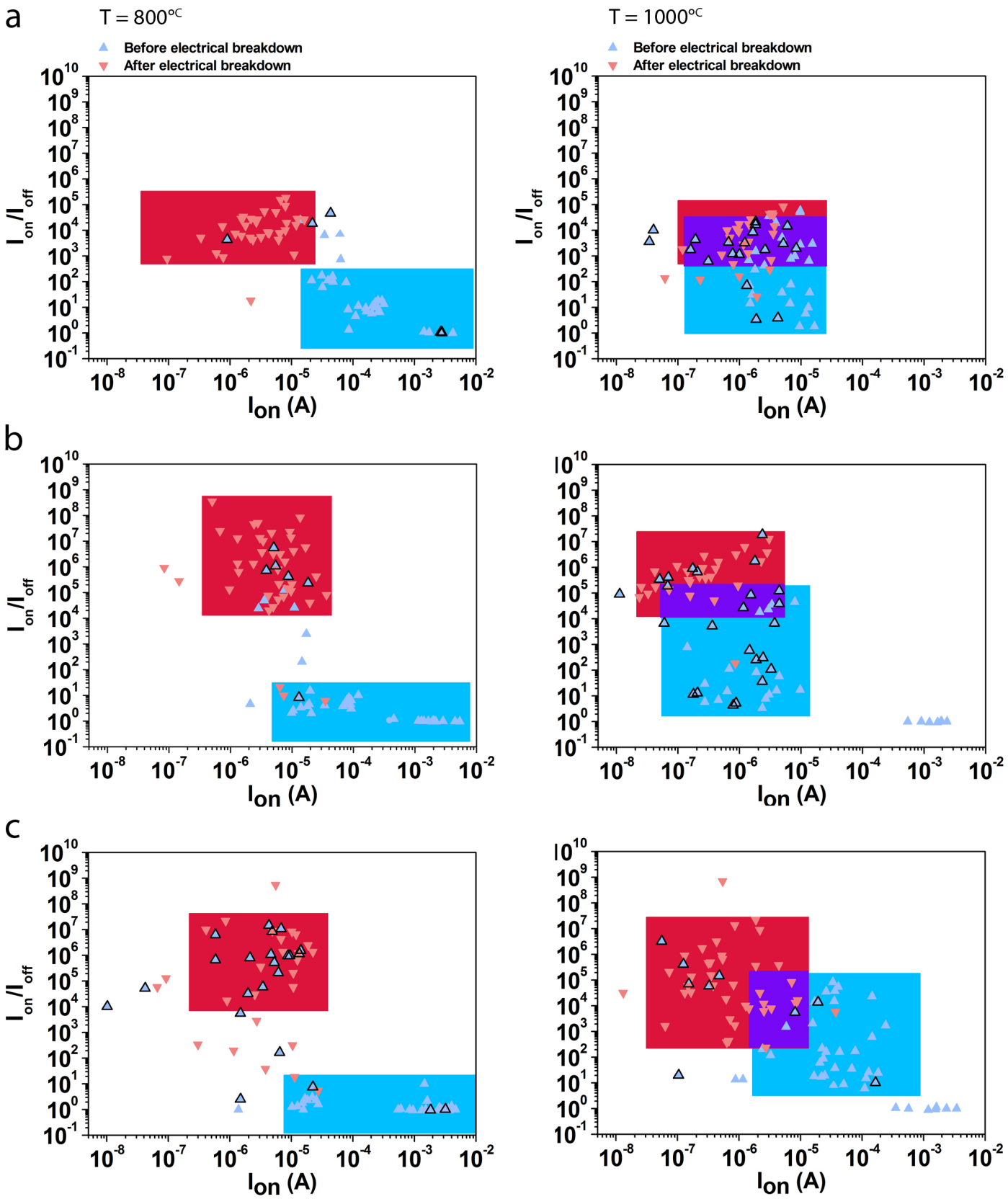

Fig. 6 Ion/Ioff ratios of FET-devices fabricated with SWCNTs from (a) FeRu catalysts (b) CoRu catalysts and (c) NiRu catalysts, at (left) 800°C and (right) 1000°C. The blue points correspond to the results obtained before any electrical breakdown while the red points correspond to the results obtained after the electrical breakdown. Black points indicate the transistors where the electrical breakdown process was found to be ineffective.

3 Experimental section

3.1 Synthesis of the Prussian blue analogs (pre-catalyst)

An aqueous solution containing the hexa-aquo complex $[\mathrm{M(H2O)}]^{6}_{2+}$ (5 mM) and cesium chloride (5 mM) (CsCl) (CoRu and NiRu system) or potassium chloride (KCl for FeRu system) (5mM), was added to an aqueous solution containing the potassium hexacyanometallate $\mathrm{K_4Ru(CN)_6}$ salt (5 mM).

3.2 SWCNT growth

The synthetis method used in this work has been detailed in previous work[43]. Briefly, the surface of a $\mathrm{SiO_2/Si}$ wafer was first covered with a self-assembled monolayer (SAM) of a pyridine-functionalized silane. Then, the bimetallic (FeRu, CoRu and NiRu) PBA NPs were assembled by coordination bonds on the pre-formed organic SAM. A 5-minute pretreatment under activated hydrogen in the CVD chamber allowed the reduction of the PBA NPs into bimetallic NPs, which is the effective catalyst for the SWCNT growth. The resulting alloy NPs were then used to catalyze SWCNT growth via $\mathrm{CH_4/H_2}$ double hot-filament chemical vapor deposition (d-HFCVD) (growth time is 30 minutes). For the present study, syntheses (pretreatment, and subsequent growth) were performed at four different temperatures (700°C, 800°C, 900°C, and 1000°C) for each catalyst. For each synthesis temperature, the synthesis of SWCNTs was performed on three samples (one of each catalyst) at the same time. Under this condition, we ensure to analyze the effect of the synthesis temperature on the SWCNT structure for a given catalyst or the effect of the catalyst chemical composition for a fixed growth temperature.

3.3 Electrode deposition

UV-lithography was used to deposit palladium electrodes. First, the $\mathrm{SiO_2/Si}$ substrate with SWCNTs was cleaned in a sonication bath for three minutes in acetone, and isopropanol, subsequently. Then, photosensitive resin $\mathrm{SU_8}$ was spin-coated (30 seconds at 4000 rpm) and the wafer was annealed for 5 minutes at 110°C. A patterned quartz mask was used to allow selective UV-illumination. The sample was illuminated for 7 seconds at 10 mW by a UV-light. The sample was then immersed for 25 seconds in a solution of MF 319, where the UV-exposed resin was removed. Then, the sample was transferred to an evaporator system to undergo the deposition of 40 nm of palladium. Finally, the sample was placed in a boiling acetone solution for a few minutes, the remaining photoresin covered by metal, was removed. The wafer was then rinsed in a boiling isopropanol solution.

3.4 Electrical breakdown of m-SWCNTs

We used the electrical breakdown method developed by IBM[27] to selectively disconnect metallic SWCNTs. During the process the s-SWCNTs are protected by depleting them from their carriers, through the application of an adapted gate voltage to set the FET device in its Off state and then a high voltage is applied between source and drain. Here we fixed the gate voltage at 25 V and the voltage between source and drain varied gradually between 0 and 25 V.

3.5 Nanoparticle characterization

Diameter distributions of the catalyst NPs were obtained through TEM imaging. Catalyst NPs after pretreatment or after growth are transferred onto a TEM grid according to a process previously described[43]. Then, TEM imaging was performed using an image-corrected FEI TITAN environmental TEM (ETEM) operating at 300 kV.

3.6 SWCNT characterization

Diameter distributions along with the SC/M ratio of the as-grown SWCNT samples were determined using Raman spectroscopy performed on a HORIBA LabRam ARAMIS spectrometer, using a x 100 objective, with four excitation wavelengths (473 nm, 532 nm, 633 nm, and 785 nm). The spectra were acquired for 1s using a 1800 groove per mm grating, giving a spectral resolution of 0.7 cm^{-1}. The spectrometer was calibrated for a Si signal at 520.7 cm^{-1}. For all samples and at each wavelength, at least three mappings (50 x 50 μm, with a 5 μm step in both directions, which amounted to a total of 121 recorded spectra per mapping) were carried out on the substrate. For each sample, all the statistics have been made on around 200 peaks, adjutsting the number of mapping to fit this criterium (same number for each laser). Concerning the counting of carbon nanotubes, we obtained well-defined individual radial breathing mode (RBM) peaks, then each identified individual peak (with an intensity higher than three times the background intensity) was counted as one SWCNT. They were fitted with a Lorentzian profile, and their frequency was measured. In order to extract a nanotube diameter from its RBM peak frequency, we used the empirical law reported by Jorio and co-workers[58], for SWCNTs grown supported on $\mathrm{SiO_2}$ ωRBM = 248/dt, where ωRBM is the resonance frequency of the nanotube expressed in cm^{-1}, and dt is the tube diameter expressed in nanometers. With the diameter of the nanotube and knowing the excitation energy an adapted Kataura plot was used[59,60] to determine the semiconducting or metallic character. The HRTEM images of SWCNTs were taken with an image-corrected FEI TITAN environmental TEM (ETEM) and a Cs-corrected Jeol ARM 200F microscope, both operating at 80kV.

3.7 Electrical measurements

Electrical measurements were performed using a Keithley 4200 SCS. For all measurements, a fixed bias voltage of 1V was applied between source and drain (Vds). A voltage sweep was applied from -40V to +40V to the gate (Vg) electrode and we measured the current flowing between source and drain (Ids).

4 Conclusions

In this work, three bimetallic catalyst systems were studied, all of which were prepared by the same process and obtained with identical morphologies and distributions. The stability of the catalyst diameter distribution throughout the growth process was demonstrated by the TEM statistical analysis. A statistical analysis of the nanotubes' diameter distribution performed by multiwavelength Raman spectroscopy shows a global shift of distributions towards

larger diameters with increasing temperature. Assuming a tangential growth mode, based on TEM images of SWCNT attached to catalyst nanoparticles after growth, we were able to establish a link between the evolution of diameter distributions, not with an increase in the size of the catalyst NPs, but rather with a phenomenon of selective activation of different catalyst size populations in the same initial pool of available catalysts by tuning the growth temperature. We assume that this effect can be correlated with the difference in carbon solubility in NPs according to their size and chemical composition and propose a phenomenological model. Indeed, the role of ruthenium is twofold because it makes it possible to limit the carbon concentration in NPs and thus to promote a tangential mode. In addition, the carbon concentration in the NPs can be modulated to obtain a more precise control of the tubes produced. Further, using a Raman characterization of our samples, confirmed by a statistical analysis of FET devices, we have evidenced a temperature evolution of the SC/M ratio, that we analyse as being a direct consequence of the diameter tuning in our etching synthesis conditions. Finally, with an appropriate choice of the growth temperature, the devices manufactured have shown performance at the state of the art. Our work is therefore a first step to better understand why bimetallic catalysts are so interesting for the growth of SWCNTs and how to adjust their properties in order to obtain a more selective synthesis. It provides a rational understanding of the key factors that determine SWCNT diameters, providing new elements to grow SWCNTs with defined chiralities.

Conflicts of interest

There are no conflicts to declare.

Acknowledgements

The research leading to these results has received funding from the French Research Funding Agency under grant No. ANR-13-BS10-0015 (SYNAPSE project), the European Union Seventh Framework Programme (FP7/ 2007e2013) under grant agreement 604472 (IRENA project), Tempos-NanoTEM and TEMPOS NanoMax under the reference ANR-10-EQPX-50 and the Chaire de Recherche André Citroen (PSA AC3M) at Ecole Polytechnique (France). The authors thank the METSA research foundation for giving access to the Cs-corrected TEM of MPQ-Paris Diderot laboratory.

Notes and references

1 M. S. Dresselhaus, G. Dresselhaus and P. Avouris, *Carbon Nanotubes*, Springer: Berlin, Heidelberg, 2001.

2 S. M. Bachilo, L. Balzano, J. E. Herrera, F. Pompeo, D. E. Resasco and R. B. Weisman, *J. Am. Chem. Soc.*, 2003, **125**, 11186–11187.

3 Y. Miyauchi, S. Chiashi, Y. Murakami, Y. Hayashida and S. Maruyama, *Chem. Phys. Lett.*, 2004, **387**, 198 – 203.

4 X. Li, X. Tu, S. Zaric, K. Welsher, W. S. Seo, W. Zhao and H. Dai, *J. Am. Chem. Soc.*, 2007, **129**, 15770–15771.

5 M. He, A. I. Chernov, P. V. Fedotov, E. D. Obraztsova, J. Sainio, E. Rikkinen, H. Jiang, Z. Zhu, Y. Tian, E. I. Kauppinen, M. Niemelä and A. O. I. Krause, *J. Am. Chem. Soc.*, 2010, **132**, 13994–13996.

6 M. He, P. V. Fedotov, A. Chernov, E. D. Obraztsova, H. Jiang, N. Wei, H. Cui, J. Sainio, W. Zhang, H. Jin, M. Karppinen, E. I. Kauppinen and A. Loiseau, *Carbon*, 2016, **108**, 521 – 528.

7 H. Wang, L. Wei, F. Ren, Q. Wang, L. D. Pfefferle, G. L. Haller and Y. Chen, *ACS Nano*, 2013, **7**, 614–626.

8 J. R. Sanchez-Valencia, T. Dienel, O. Gröning, I. Shorubalko, A. Mueller, M. Jansen, K. Amsharov, P. Ruffieux and R. Fasel, *Nature*, 2014, **512**, 61.

9 F. Yang, X. Wang, D. Zhang, J. Yang, D. Luo, Z. Xu, J. Wei, J.-Q. Wang, Z. Xu, F. Peng, X. Li, R. Li, Y. Li, M. Li, X. Bai, F. Ding and Y. Li, *Nature*, 2014, **510**, 522.

10 S. Zhang, L. Kang, X. Wang, L. Tong, L. Yang, Z. Wang, K. Qi, S. Deng, Q. Li, X. Bai, F. Ding and J. Zhang, *Nature*, 2017.

11 F. Yang, X. Wang, D. Zhang, K. Qi, J. Yang, Z. Xu, M. Li, X. Zhao, X. Bai and Y. Li, *J. Am. Chem. Soc.*, 2015, **137**, 8688–8691.

12 F. Yang, X. Wang, J. Si, X. Zhao, K. Qi, C. Jin, Z. Zhang, M. Li, D. Zhang, J. Yang, Z. Zhang, Z. Xu, L.-M. Peng, X. Bai and Y. Li, *ACS Nano*, 2017, **11**, 186–193.

13 V. Jourdain and C. Bichara, *Carbon*, 2013, **58**, 2 – 39.

14 F. Yang, X. Wang, M. Li, X. Liu, X. Zhao, D. Zhang, Y. Zhang, J. Yang and Y. Li, *Accounts of Chemical Research*, 2016, **49**, 606–615.

15 H. An, A. Kumamoto, H. Takezaki, S. Ohyama, Y. Qian, T. Inoue, Y. Ikuhara, S. Chiashi, R. Xiang and S. Maruyama, *Nanoscale*, 2016, **8**, 14523–14529.

16 X. Wang, M. He and F. Ding, *Materials Today*, 2018, **21**, year.

17 M. He, S. Zhang, Q. Wu, H. Xue, B. Xin, D. Wang and J. Zhang, *Advanced Materials*, 2018, 1800805.

18 E. S. Penev, K. V. Bets, N. Gupta and B. I. Yakobson, *Nano Letters*, 2018, **18**, 5288–5293.

19 M. He, H. Jin, L. Zhang, H. Jiang, T. Yang, H. Cui, F. Fossard, J. B. Wagner, M. Karppinen, E. I. Kauppinen and A. Loiseau, *Carbon*, 2016, **110**, 243 – 248.

20 A. R. Harutyunyan, G. Chen, T. M. Paronyan, E. M. Pigos, O. A. Kuznetsov, K. Hewaparakrama, S. M. Kim, D. Zakharov, E. A. Stach and G. U. Sumanasekera, *Science*, 2009, **326**, 116–120.

21 G. Hong, B. Zhang, B. Peng, J. Zhang, W. M. Choi, J.-Y. Choi, J. M. Kim and Z. Liu, *Journal of the American Chemical Society*, 2009, **131**, 14642–14643.

22 B. Yu, C. Liu, P.-X. Hou, Y. Tian, S. Li, B. Liu, F. Li, E. I. Kauppinen and H.-M. Cheng, *J. Am. Chem. Soc.*, 2011, **133**, 5232–5235.

23 X. Qin, F. Peng, F. Yang, X. He, H. Huang, D. Luo, J. Yang, S. Wang, H. Liu, L. Peng and Y. Li, *Nano Lett.*, 2014, **14**, 512–517.

24 L. Ding, A. Tselev, J. Wang, D. Yuan, H. Chu, T. P. McNicholas, Y. Li and J. Liu, *Nano Lett.*, 2009, **9**, 800–805.

25 W.-S. Li, P.-X. Hou, C. Liu, D.-M. Sun, J. Yuan, S.-Y. Zhao, L.-C. Yin, H. Cong and H.-M. Cheng, *ACS Nano*, 2013, **7**, 6831–6839.

26 F. Zhang, P.-X. Hou, C. Liu, B.-W. Wang, H. Jiang, M.-L. Chen,

D.-M. Sun, J.-C. Li, H.-T. Cong, E. I. Kauppinen and H.-M. Cheng, *Nat. Commun.*, 2016, **7**, 11160.
27 P. G. Collins, M. S. Arnold and P. Avouris, *Science*, 2001, **292**, 706–709.
28 W. Wang, X. Bai, Z. Xu, S. Liu and E. Wang, *Chem. Phys. Lett.*, 2006, **419**, 81 – 85.
29 K. Tanioku, T. Maruyama and S. Naritsuka, *Diam. Relat. Mater.*, 2008, **17**, 589 – 593.
30 N. Li, X. Wang, F. Ren, G. L. Haller and L. D. Pfefferle, *J. Phys. Chem. C*, 2009, **113**, 10070–10078.
31 C. Zoican Loebick, R. Podila, J. Reppert, J. Chudow, F. Ren, G. L. Haller, A. M. Rao and L. D. Pfefferle, *J. Am. Chem. Soc.*, 2010, **132**, 11125–11131.
32 C. Lu and J. Liu, *J. Phys. Chem. B*, 2006, **110**, 20254–20257.
33 M. Picher, E. Anglaret, R. Arenal and V. Jourdain, *Nano Lett.*, 2009, **9**, 542–547.
34 M. Picher, E. Anglaret, R. Arenal and V. Jourdain, *ACS Nano*, 2011, **5**, 2118–2125.
35 M. Diarra, A. Zappelli, H. Amara, F. Ducastelle and C. Bichara, *Phys. Rev. Lett.*, 2012, **109**, 1–5.
36 Y. Magnin, A. Zappelli, H. Amara, F. Ducastelle and C. Bichara, *Phys. Rev. Lett.*, 2015, **115**, 1–5.
37 M. F. C. Fiawoo, A. M. Bonnot, H. Amara, C. Bichara, J. Thibault-Pénisson and A. Loiseau, *Phys. Rev. Lett.*, 2012, **108**, 1–5.
38 H. Amara and C. Bichara, *Top. Curr. Chem.*, 2017, **375**, 55.
39 M. He, Y. Magnin, H. Jiang, H. Amara, E. I. Kauppinen, A. Loiseau and C. Bichara, *Nanoscale*, 2018, **10**, 6744–6750.
40 R. Yang, P. Goethel, J. Schwartz and C. Lund, *J. Catal.*, 1990, **122**, 206 – 210.
41 S. Hallstrom, *Journal of Phase Equilibria & Diffusion*, 2004, **25**, 252–254.
42 T. B. Massalski, *Binary Alloy Phase Diagrams, 2nd Edition*, ASM International, 1990.
43 A. Castan, S. Forel, L. Catala, I. Florea, F. Fossard, F. Bouanis, A. Andrieux-Ledier, S. Mazerat, T. Mallah, V. Huc, A. Loiseau and C. Cojocaru, *Carbon*, 2017, **123**, 583 – 592.
44 L. Catala and T. Mallah, *Coord. Chem. Rev.*, 2017, **346**, 32 – 61.
45 P. Voorhees, *J. Stat. Phys.*, 1985, **38**, 231–252.
46 H. J. Jeong, L. Eude, M. Gowtham, B. Marquardt, S. H. Lim, S. Enouz, C. S. Cojocaru, K. A. Park, Y. H. Lee and D. Pribat, *Nano*, 2008, **03**, 145–153.
47 F. Z. Bouanis, C. S. Cojocaru, V. Huc, E. Norman, M. Chaigneau, J.-L. Maurice, T. Mallah and D. Pribat, *Chem. Mater.*, 2014, **26**, 5074–5082.
48 Y. Shibuta and S. Maruyama, *Chem. Phys. Lett.*, 2003, **382**, 381 – 386.
49 J. Zhao, A. Martinez-Limia and P. B. Balbuena, *Nanotechnology*, 2005, **16**, S575.
50 M. He, H. Amara, H. Jiang, J. Hassinen, C. Bichara, R. H. A. Ras, J. Lehtonen, E. I. Kauppinen and A. Loiseau, *Nanoscale*, 2015, **7**, 20284–20289.
51 F. Ding and K. Bolton, *Nanotechnology*, 2006, **17**, 543.
52 M. Diarra, H. Amara, F. Ducastelle and C. Bichara, *Physica Status Solidi (B) Basic Research*, 2012, **249**, 2629–2634.
53 H. Navas, M. Picher, A. Andrieux-Ledier, F. Fossard, T. Michel, A. Kozawa, T. Maruyama, E. Anglaret, A. Loiseau and V. Jourdain, *ACS Nano*, 2017, **11**, 3081–3088.
54 J.-M. Aguiar-Hualde, Y. Magnin, H. Amara and C. Bichara, *Carbon*, 2017, **120**, 226–232.
55 G. J. Brady, A. J. Way, N. S. Safron, H. T. Evensen, P. Gopalan and M. S. Arnold, *Science Advances*, 2016, **2**, e1601240–e1601240.
56 P. Laiho, K. Mustonen, Y. Ohno, S. Maruyama and E. I. Kauppinen, *ACS Applied Materials and Interfaces*, 2017, **9**, 20738–20747.
57 D.-m. Sun, M. Y. Timmermans, Y. Tian, A. G. Nasibulin, E. I. Kauppinen, S. Kishimoto, T. Mizutani and Y. Ohno, *Nature Nanotechnology*, 2011, **6**, 156–161.
58 A. Jorio, R. Saito, J. H. Hafner, C. M. Lieber, M. Hunter, T. McClure, G. Dresselhaus and M. S. Dresselhaus, *Physical Review Letters*, 2001, **86**, 1118–1121.
59 K. Sato, R. Saito, J. Jiang, G. Dresselhaus and M. S. Dresselhaus, *Physical Review B*, 2007, **76**, 195446.
60 A. R. T. Nugraha, R. Saito, K. Sato, P. T. Araujo, A. Jorio and M. S. Dresselhaus, *Applied Physics Letters*, 2010, **97**, 091905.